

Dataset description for:

Predicting the efficiency of oxygen-evolving electrolysis on the Moon and Mars

Bethany A. Lomax^{1,2*}, Gunter H. Just³, Patrick J. McHugh¹, Paul K. Broadley³, Greg C. Hutchings³, Paul A. Burke⁴, Matthew J. Roy³, Katharine L. Smith³, Mark D. Symes^{1*}

¹ *WestCHEM, School of Chemistry, University of Glasgow, Glasgow, G12 8QQ, United Kingdom*

² *European Space Research and Technology Centre, Keplerlaan, Noordwijk, 2201 AZ, Netherlands*

³ *Department of Mechanical, Aerospace and Civil Engineering, University of Manchester, Oxford Road, Manchester, M13 9PL, United Kingdom*

⁴ *Space Exploration Sector, Johns Hopkins University Applied Physics Laboratory, Laurel, Maryland, United States of America*

*Email: beth.lomax@esa.int; mark.symes@glasgow.ac.uk

Abstract: Establishing a permanent human presence on the Moon or Mars requires a secure supply of oxygen for life support and refueling. The electrolysis of water has attracted significant attention in this regard as water-ice may exist on both the Moon and Mars. However, to date there has been no study examining how the lower gravitational fields on the Moon and Mars might affect gas-evolving electrolysis when compared to terrestrial conditions. Herein we provide experimental data on the effects of gravitational fields on water electrolysis from 0.166 g (lunar gravity) to 8 g (eight times the Earth's gravity) and show that electrolytic oxygen production is reduced by around 11% under lunar gravity with our system compared to operation at 1 g. Moreover, our results indicate that electrolytic data collected using less resource-intensive ground-based experiments at elevated gravity (>1 g) may be extrapolated to gravitational levels below 1 g.

Methods

Hyper-gravity experiments from 1 to 8 g were conducted in a laboratory setting using a short-arm centrifuge (radius = 25 cm); two cells on opposite arms were used to collect data. An orbital shaking plate (Orbital Incubator STUART SI 50) operating between 0 and 200 RPM was used to examine the relationship between electrolysis efficiency and vibration/shaking motions in the studied system.

Reduced-gravity electrolysis experiments between 0 and 1 g were carried out on Novespace's Airbus A310 aircraft. Data were collected over three flights consisting of 30 microgravity parabolas each. The microgravity level achieved during parabolic flight is approximately 10^{-2} g. A rotating short-arm centrifuge (the same system as used for the hypergravity experiments) equipped with four electrochemical cells was operated during the microgravity flights to create artificial reduced-gravity; two additional cells were housed separately to the centrifuge and were kept stationary for the duration of the microgravity flights. The minimum duration of reduced gravity was approximately 22 seconds; as such all experiments were carried out for 18 seconds to ensure completion prior to the parabola exit maneuver.

Centrifuge experiment set-up

The experiment rack was designed to comply with Novespace's safety, interface, and design requirements and is shown in Supplementary Figure 1 (see also Supplementary Note 1). Four electrolysis cells were attached to a centrifuge (radius = 25 cm), as shown in Supplementary Figure 2. Baskets were attached to each arm of the centrifuge with low-friction ceramic bearings (SMB Bearings CCZR-696PK) and a stainless steel pin. Baskets were free-swinging in all hypergravity experiments, and locked in place horizontally with 3D-printed PLA (polylactic acid) inserts for all reduced-gravity experiments. The centrifuge table structure was affixed on vibration dampening pads (Ganter GN148-60-M10-A-1-57) to decouple the vibrations of the aircraft from the experiment.

A hollow aluminium shaft was attached to the table structure with two bearings (NSK PSF30CR) and rotated using a bi-directional stepper motor (Oriental motors PK5913HNAW with Oriental motors CVD528B-K motor driver). The motor driver was controlled by a PID (proportional integral derivative) closed feedback loop, utilizing a 3-axis accelerometer (DFRobot SENO142) positioned at the center of one cell basket to ensure the desired artificial gravity was maintained throughout an experiment. A through-bore, 42-circuit gold-gold contact slip ring (Senring H3099-42S-D-52824) enclosing the shaft fed all power and data cables to the rotating system. All cables were fed through a

braided metal shielding sleeve and/or a metal conduit to minimize signal interference. Two 3D-printed PLA camera holders were attached to each basket and contained an action camera (AKASO V50 X), each fitted with a 15× macro lens to observe the front and side of each working electrode. Footage was recorded at 60 frames per second with a resolution of 1080p. A battery powered LED strip was fitted around the basket to illuminate the electrode from all sides. Two additional cells were attached to a stationary table on vibration dampening pads (Ganter GN356-25-20-20-SS-55) next to the centrifuge for microgravity data collection during flight. A Type K thermocouple (RS PRO 397-1488) was attached to the outer wall of one stationary cell.

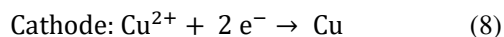
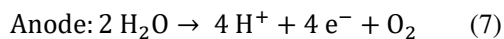
Electrochemical cell

Electrochemical cells (Figure 9) were custom-designed and machined from polycarbonate, with internal dimensions of 40 × 40 × 28 mm (X × Z × Y; anodic chamber) and 40 × 40 × 21 mm (X × Z × Y; cathodic chamber). The lid was sealed with a silicone gasket and 12 bolts to ensure each cell was liquid and gas-tight. The anodic and cathodic chambers were separated by a 25 × 25 mm Nafion™ N-117 ion exchange membrane (Alfa Aesar, 0.180 mm thick) sandwiched between two polycarbonate windows with two silicone gaskets on either side. The entire assembly was sealed with silicone gel within a groove in the cell walls to limit electrolyte mixing. Vertical polycarbonate electrode holders were suspended from the cell roof parallel to the membrane. The counter electrode was orientated towards the membrane, while the working electrode was orientated towards the cell wall so that the surface of interest could be observed. The anodic chamber lid contained feedthroughs for the working electrode wire (which was subsequently connected to a 2 mm banana socket), an IP68 rated cable gland for the reference electrode, a 0-50 mbar gauge pressure sensor with a ±0.25% full range accuracy (Cynergy3 IPSL-G0050-5M12/PRO), and a direct-acting 2/2-way solenoid pressure release valve (Bürkert 00290108). The cathodic chamber lid was fitted with a counter electrode wire feedthrough connected to a 2 mm banana socket, and a membrane vent rated to 300 mL/min (Amphenol LTW, VENT-PS2NBK-O8001).

Electrochemical system

Electrolysis was carried out both galvanostatically and potentiostatically with a three-electrode system to investigate the impact of gravity on an oxygen-evolving working electrode. 5 M sulfuric acid (titration grade, VWR Chemicals), anhydrous copper sulfate (98%, Alfa Aesar), and HPLC grade water were used to prepare both electrolyte solutions (total volume of 69 mL). The cathodic electrolyte (32 mL) consisted of copper sulfate (1.135 M) in dilute sulfuric acid (0.75 M), while the anodic electrolyte (37 mL) was dilute sulfuric acid (0.75 M). The anodic and cathodic reactions are

given by Equations (7) and (8) respectively. Copper sulfate was chosen for the cathodic electrolyte to suppress hydrogen production on the aircraft (necessary for regulatory reasons); the anodic electrolyte was free from copper sulfate for improved electrode preservation and observation.



Gold foil (0.025 mm thick, Premion 99.985%, Alfa Aesar) cut to 1.25×1.25 cm (giving an electrode area of 1.56 cm^2) was used as the anode in all experiments, while copper foil (0.025 mm thick, annealed uncoated, 99.8%, Alfa Aesar) of equivalent size was used as the cathode in all experiments. New electrodes were used for each parabolic flight (an experiment set of 30 data points). A tin-coated copper wire was soldered to the back of each electrode and fed through the electrode holders and cell lids. Electrodes were fixed flat on the surface of polycarbonate electrode holders using a two-part epoxy glue (Gorilla Glue); the wire and solder assembly was embedded into an epoxy-filled groove machined into the polycarbonate. The embedded wire was then covered with silicone to ensure that the square electrode was the only electroactive metallic surface. An Ag/AgCl gel electrolyte reference electrode (Pine Research; length: 60 mm, OD: 3.5 mm) designed for aqueous systems and fitted with a ceramic frit was used for all experiments. The electrode design and arrangement are shown in Figure 9. Electrochemical Impedance Spectroscopy (EIS) was performed under the following experimental parameters: starting frequency = 200 kHz, ending frequency = 100 mHz, DC bias = 0, 0.75, 0.85 V (vs. the open circuit potential), AC excitation amplitude = 10 mV. The series resistance, R_s , was taken as the high frequency intercept on the x-axis of the resulting Nyquist plot. The procedure was carried out on the cells before and after oxygen-producing bulk electrolysis, indicating an initial R_s of $\sim 0.9 \Omega$ ($\sim 1.4 \Omega \text{ cm}^2$) which, post-electrolysis at 1 g, rose to $\sim 1.0 \Omega$ ($\sim 1.56 \Omega \text{ cm}^2$). All potential values throughout this manuscript are reported without iR-compensation.

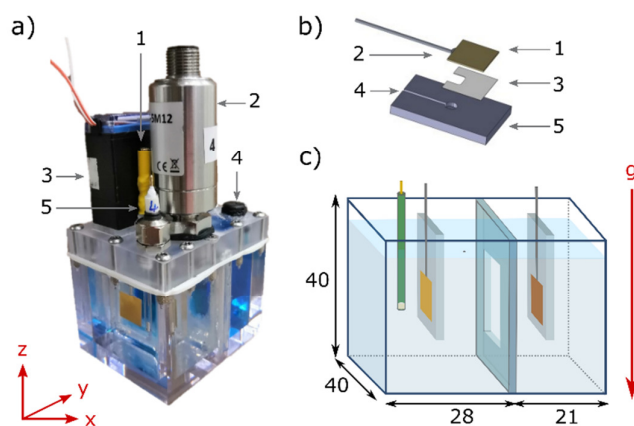


Figure 9: Electrolysis cell design. a) The polycarbonate cell showing (1) the electrode connection, (2) pressure sensor, (3) pressure release valve, (4) vent, (5) reference electrode; b) Electrode preparation method showing: (1) the foil electrode, (2) soldered wire, (3) epoxy glue layer, (4) epoxy-filled groove for wire and solder, and (5) polycarbonate electrode holder; c) the spatial arrangement of the gold anode, Ag/AgCl reference electrode (shown as green for clarity), Nafion membrane window, and copper cathode. Numbers indicate cell dimensions (in mm).

A time gap of at least three minutes was maintained between all electrochemical experiments to limit the influence of any concentration gradients that may have formed as a result of the previous experiment. The average temperature during all data sets was 21.5 °C, with a maximum variation of 2 °C across any given data set. The average pressure inside the aircraft was 856 mbar; all ground-based hypergravity experiments were conducted at ambient pressure.

System control and data acquisition

The electrolysis data were obtained using a Biologic VMP3 16-channel potentiostat. Potentiostat cable extensions on the centrifuge between the slip-ring and cells were comprised of five coaxial cables for the working lead, counter lead, working sense, counter sense, and reference lead, which were woven together and shielded further with an external braided metallic sleeve and insulating plastic sleeve. The cable design emulated that of the cables supplied with the Biologic VMP3. A MyRIO 1900 (National Instruments) microcontroller controlled via LabVIEW software (National Instruments) was used for the centrifuge control and all additional data acquisition. The MyRIO communicated with the potentiostat control computer via a WiFi connection to sync the timestamp of both computers to facilitate data analysis. Thermocouple data were logged using an independent temperature data logger (Omega HH306A). Camera data were stored on internal SD cards. The data acquisition (DAQ) and control architecture of the experiment is shown in Supplementary Figure 3.

Data analysis

The average potential or current was obtained between 4 and 18 seconds for each galvanostatic or potentiostatic experiment respectively to remove the influence of the bubble nucleation and potential/current stabilization period at the start of the electrolysis. Examples of the raw data sets are shown in Supplementary Figures 16-19. To enable comparison between data sets from different cells, and across different altered gravity platforms, the percentage change with respect to 1 g was calculated. To remove the influence of baseline shift in Figures 3 and 4, and to ensure the error bars represent the variation in the trend rather than the baseline, the data displayed are the average of this percentage change applied to the average 1 g measured across the repeats.

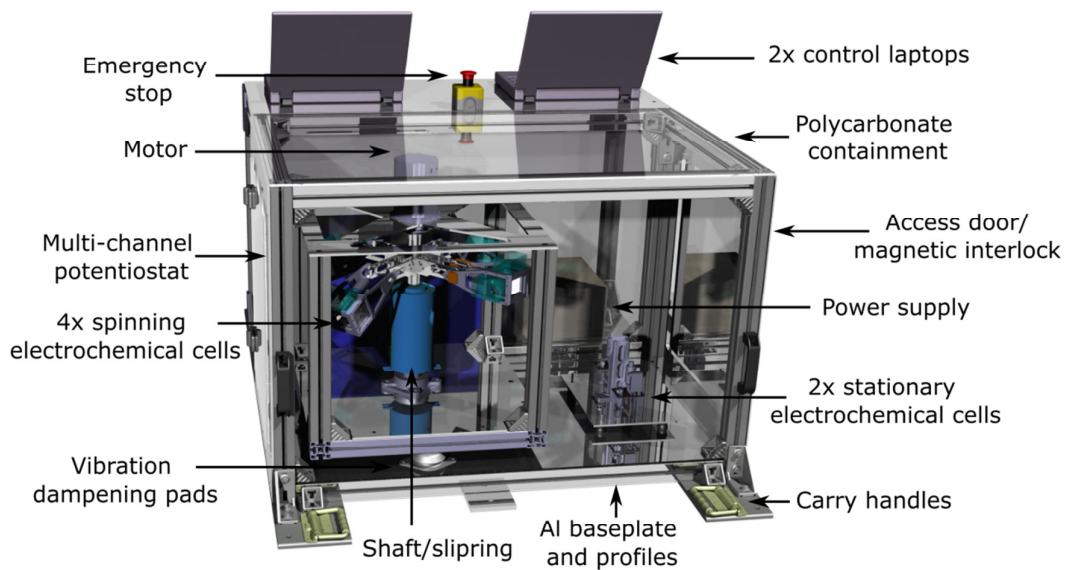
The files containing accelerometer and pressure data were trimmed to 18 seconds based on the timestamp of the corresponding electrolysis file prior to further analysis. The acceleration experienced by the cells in the z-axis was averaged across 18 seconds to give the mean g-level of a given experiment, which was then compared to the targeted g-level (Supplementary Figure 4 and Supplementary Figure 5). The g-level measured by the accelerometer data was equivalent to the g-level at the bottom edge of the square electrode. The gravity gradient across the electrode surface and in the surrounding electrolyte was calculated based on the RPM (revolutions per minute) at a given acceleration, the known distance of the accelerometer from the axis of rotation, and the increased or decreased distance to the axis of rotation at any given point across a 2D surface (Supplementary Figure 6 and Supplementary Figure 7). The change in distance was calculated assuming a horizontal basket position in all cases.

To assess the level of vibration during each experiment, a 20-point rolling average was subtracted from the raw acceleration data in all three axes to give a zero baseline. The absolute values of all deviations from this baseline (i.e. vibrations) were plotted and the sum area underneath the curve was calculated to give the sum vibrational intensity of a given axis across each experiment. An example of this procedure is shown in the Supplementary Figure 8. The sum of all three axes was taken to compare the overall motion experienced by a cell across different experiments (Supplementary Figure 9). The vibrational frequency was computed by counting all peaks during the 18 second experiment using the Python `scipy.signal` module and then calculating the peaks per second.

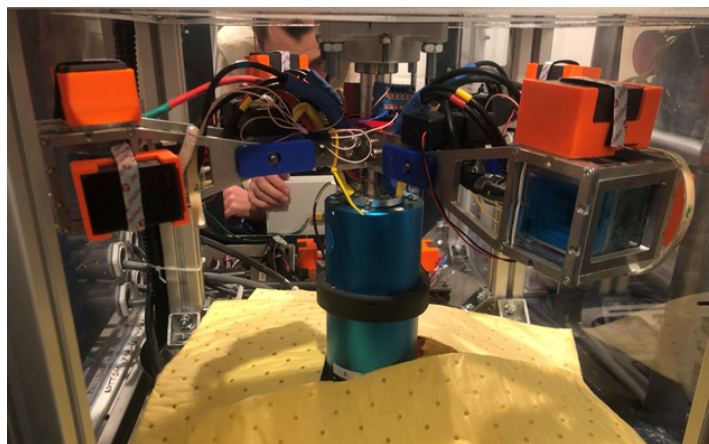
Camera footage was trimmed to 20 seconds from the key frame prior to the first frame showing bubble nucleation. Eleven frames were extracted from each experiment at two second intervals, inclusive of the first and last frame. Each set of frames was scaled and the rotation was adjusted using the known 1.25 cm electrode edge. A 1 cm² frame was cropped from the center of each electrode for comparison. Approximation of the bubble froth coverage and retention was achieved by converting

each frame (excluding 0 and 20 seconds) to grey scale and calculating the average normalized pixel color across an experiment, with 0 being black and 1 being white. To remove the influence of different lighting baselines the average percentage change relative to the average of 1 g was calculated. To compare the change in bubble attachment angle between 1 g and microgravity, frames corresponding to 6 and 16 seconds were selected from the side camera footage of a stationary cell and unhindered bubbles ($n = 16$) were selected for analysis. Here, a gas bubble submerged in liquid is investigated and thus the outside angle is of interest. Images were analyzed using the ImageJ Contact Angle plug-in. The advancing and receding attachment angles were measured three times per bubble and the results were averaged. Additional information pertaining to this measurement can be found in Supplementary Note 6.

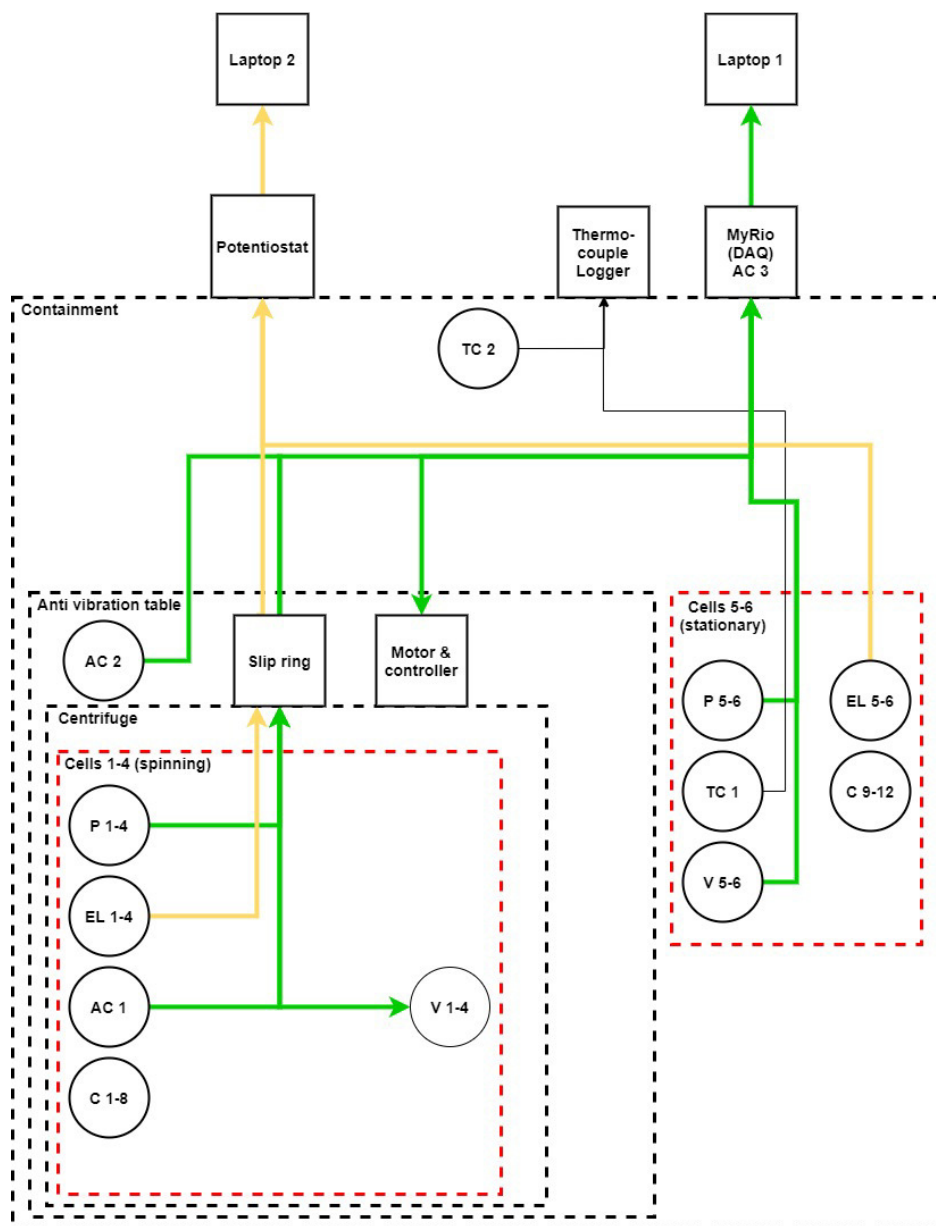
Supplementary Figures



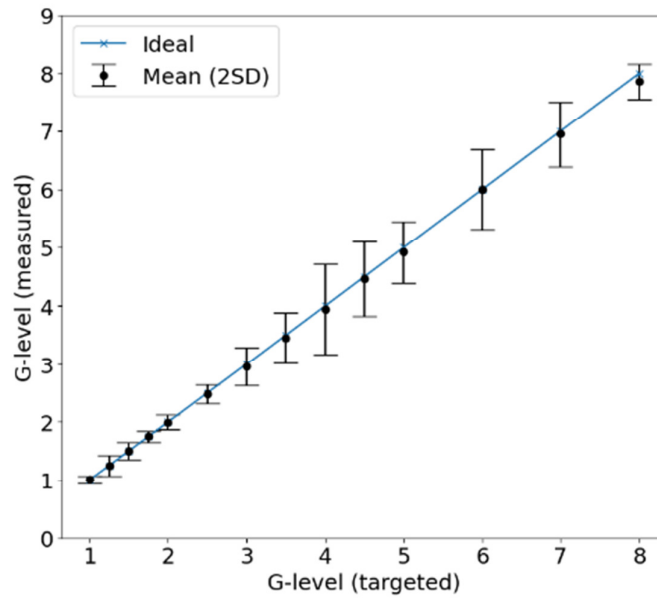
Supplementary Figure 1: CAD rendering of the rack designed for investigating altered-gravity electrolysis during parabolic flight. The locations of the centrifuge, stationary cell table, and control equipment are marked.



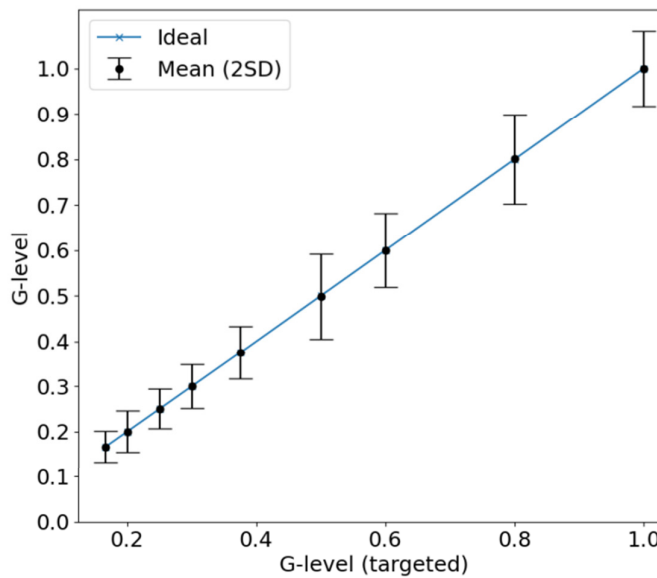
Supplementary Figure 2: The centrifuge used to create artificial gravity in flight configuration. The photograph shows the centrifuge in a locked horizontal position showing the cell baskets, the camera holders, the cabling system, and the slip-ring.



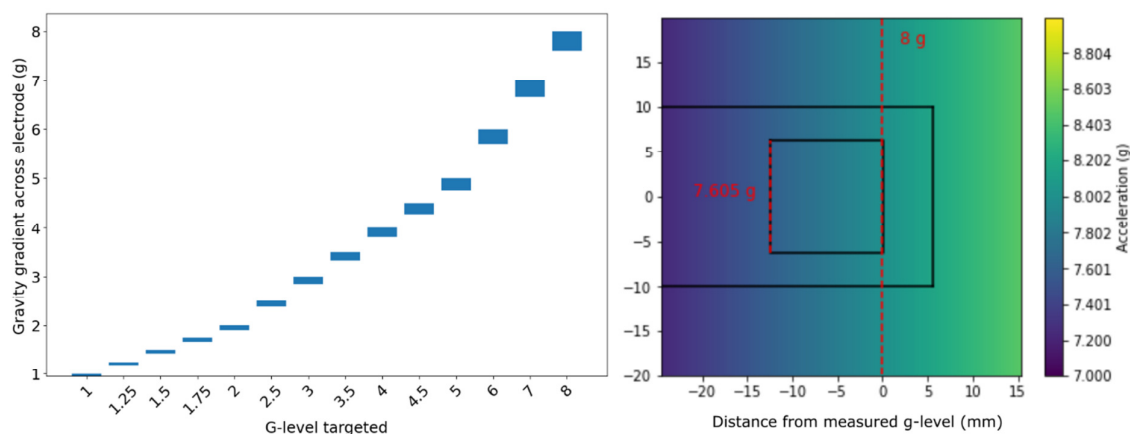
Supplementary Figure 3: Schematic of the DAQ and control system. The schematic also includes an indication of system boundaries. Green arrows indicate a connection to Laptop 1 (rack control and DAQ), orange arrows indicate connection to Laptop 2 (electrolysis control and DAQ). Input controls and data on each laptop were handled independently. AC: accelerometer; P: pressure sensor; V: release valve; EL: electrochemical cell; TC: thermocouple; C: camera.



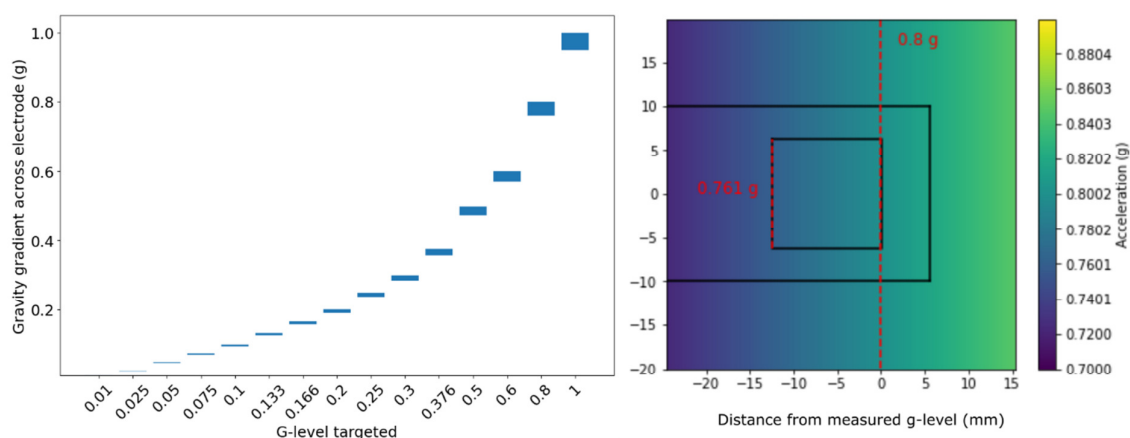
Supplementary Figure 4: Targeted vs. measured G-levels at 50 mA cm^{-2} . The measured mean artificial acceleration acting on the cell for each of the targeted g-levels on the centrifuge during data collection at 50 mA cm^{-2} . Error bars represent ± 2 standard deviations from the mean. Source data are provided as a Source Data file.



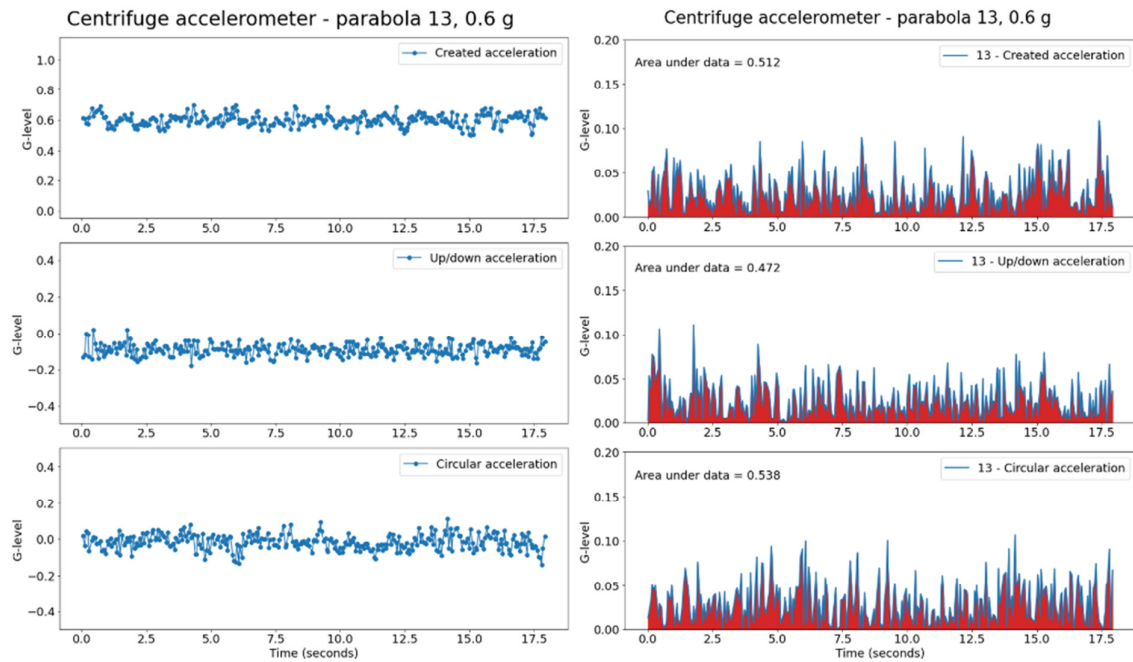
Supplementary Figure 5: Targeted vs. measured G-levels at 100 mA cm^{-2} . The measured mean artificial acceleration acting on the cell for each of the targeted reduced gravity levels on the centrifuge for a representative data set collected at 100 mA cm^{-2} ; error bars represent ± 2 standard deviations from the mean. Source data are provided as a Source Data file.



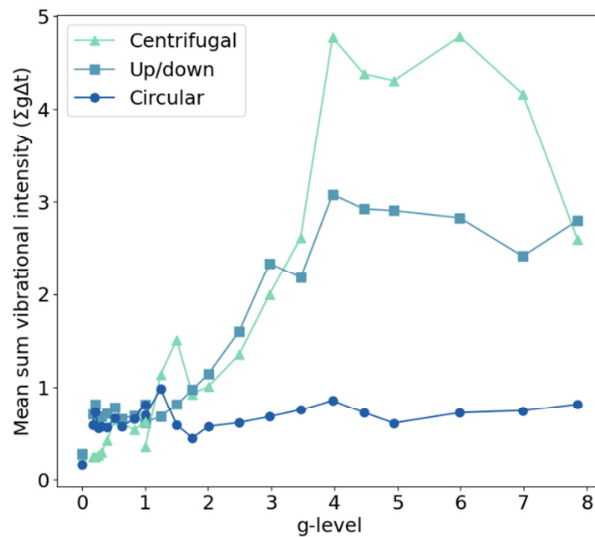
Supplementary Figure 6: Gravity gradients across the electrode for 1-8 g. The calculated gravity gradient across the gas-evolving electrode surface for each of the targeted g-levels from 1-8 g (left) and an example (8 g) of the gravity gradient calculation across an intersection of the electrolysis cell along the face of the electrode where the variation in gravity is depicted by a color bar representing ± 1 g (right). Source data are provided as a Source Data file.



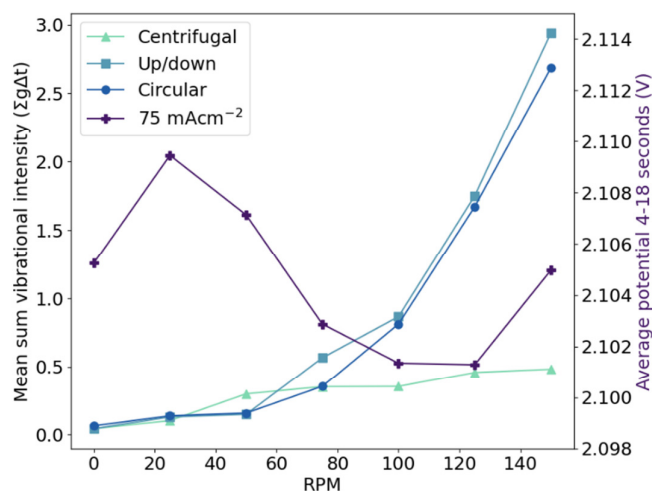
Supplementary Figure 7: Gravity gradients across the electrode for 0-1 g. The calculated gravity gradient across the gas-evolving electrode surface for each of the targeted g-levels from 0-1 g (left) and an example (0.8 g) of the gravity gradient calculation across an intersection of the electrolysis cell along the face of the electrode where the variation in gravity is depicted by a color bar representing ± 0.1 g (right). Source data are provided as a Source Data file.



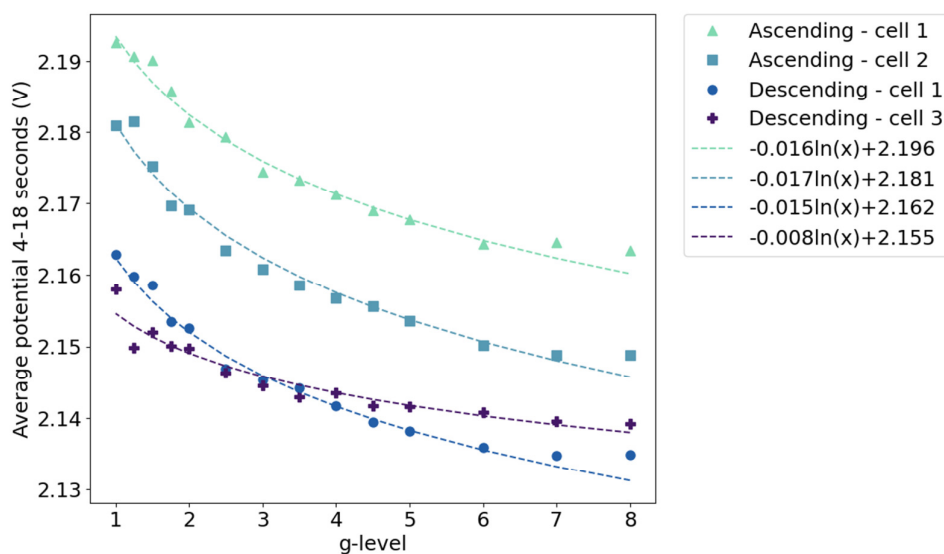
Supplementary Figure 8: Example data for vibrational analysis. The raw accelerometer data (left) and processed vibrational intensity analysis (right) for an example experiment (0.6 g , 50 mA cm^{-1}) from the centrifuge operating on the parabolic flight. The total area shown in red is used to represent the vibrational intensity. Source data are provided as a Source Data file.



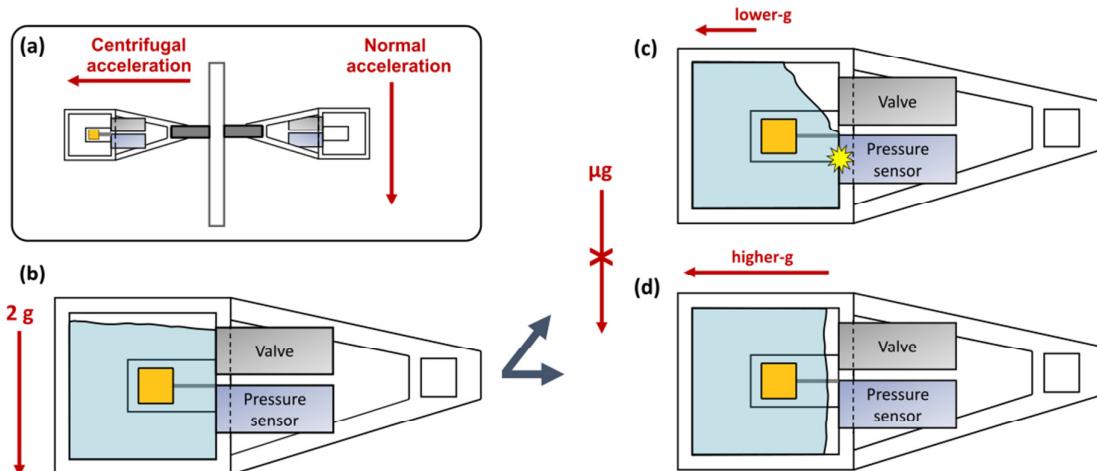
Supplementary Figure 9: comparison of the overall motion experienced by a cell across different experiments. The average sum vibrational intensity experienced by the cells in three axes during hypergravity experiments on the short-arm centrifuge. Assuming the arm is extended horizontally, the centrifugal axis is that of the created acceleration: up/down is parallel to Earth's gravity, and circular is in the plane of rotation. Source data are provided as a Source Data file.



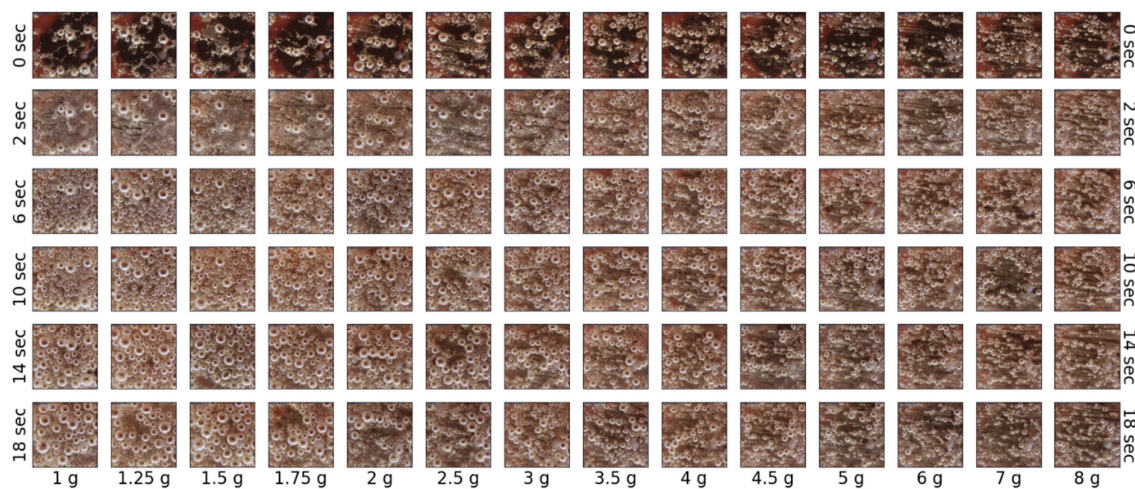
Supplementary Figure 10: The average sum vibrational intensity experienced by the cells in three axes during orbital shaker plate experiments under galvanostatic control. The vibrational data (centrifugal, up/down, and circular) is represented by the left axis, and the electrochemical data is represented by the right axis. Source data are provided as a Source Data file.



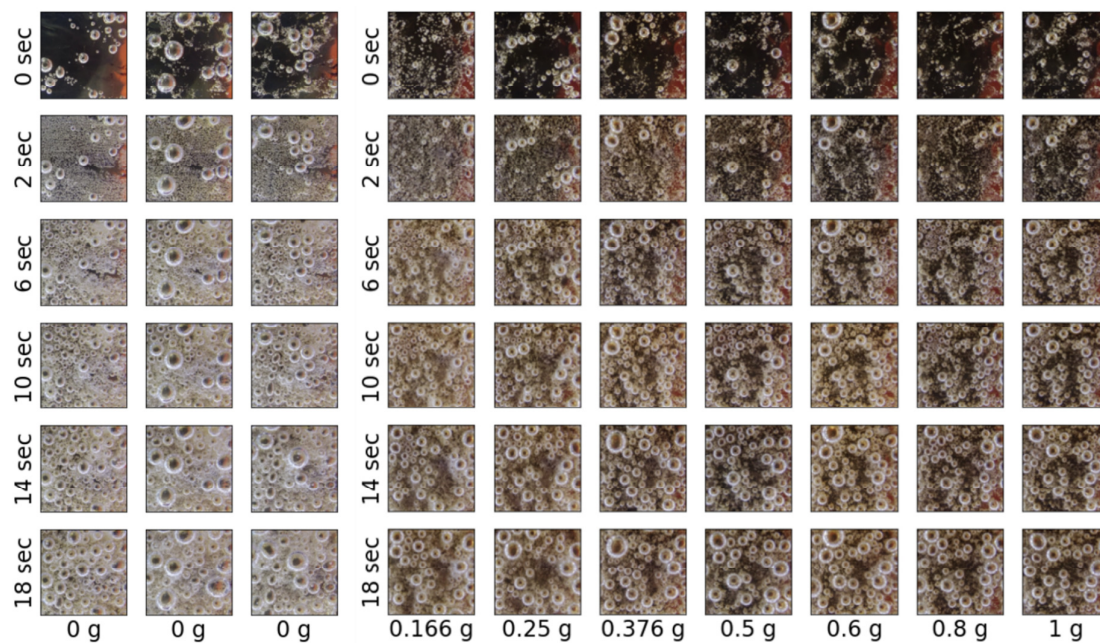
Supplementary Figure 11: Average potential vs g-level for 1-8 g. The average potential at 100 mA cm⁻² collected across 1 - 8 g with the short arm centrifuge where g-level order was either ascending (●) or descending (◻). R² values were >0.975 and >0.924 for the ascending and descending data fits respectively. Source data are provided as a Source Data file.



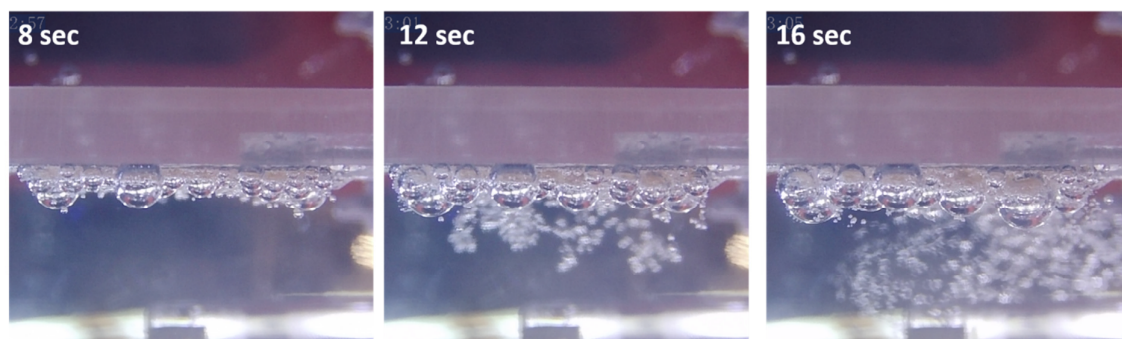
Supplementary Figure 12: Explanation of current loss via the pressure sensor ground connection at low g. The figure shows the orientation of the baskets on the centrifuge (a), the cell and baskets in the 2-g phase prior to each parabola (b), and the transition to microgravity where a low (c) or high (d) g-level is artificially created. At the lower g-levels, the centrifugal acceleration is not strong enough to overcome the surface tension between the wall and electrolyte and completely re-orientate the headspace, causing the electrolyte to contact the sensor during electrolysis.



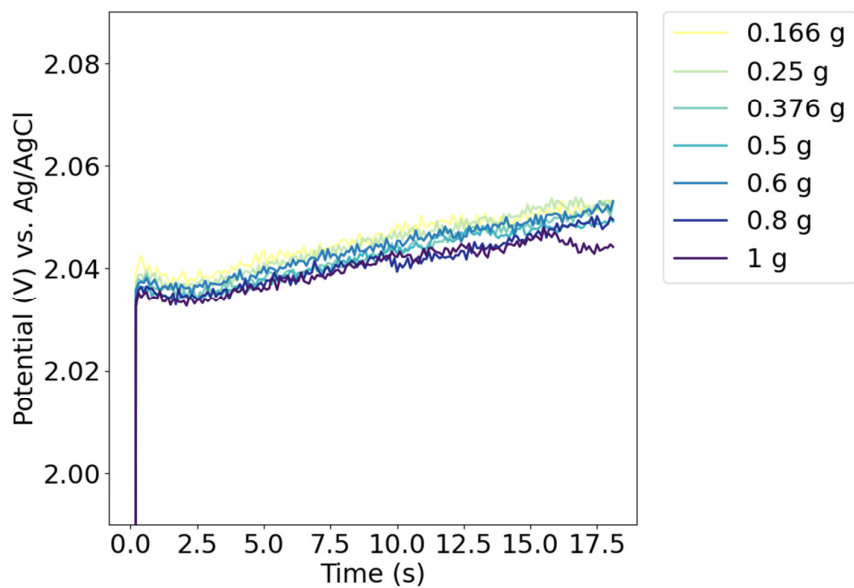
Supplementary Figure 13: Stills from video footage of the electrode at various times for 1-8 g. A comparison of 1 cm² frames of the bubbles on the electrode surface across 1 - 8 g for a 50 mA cm⁻² data set obtained on the centrifuge.



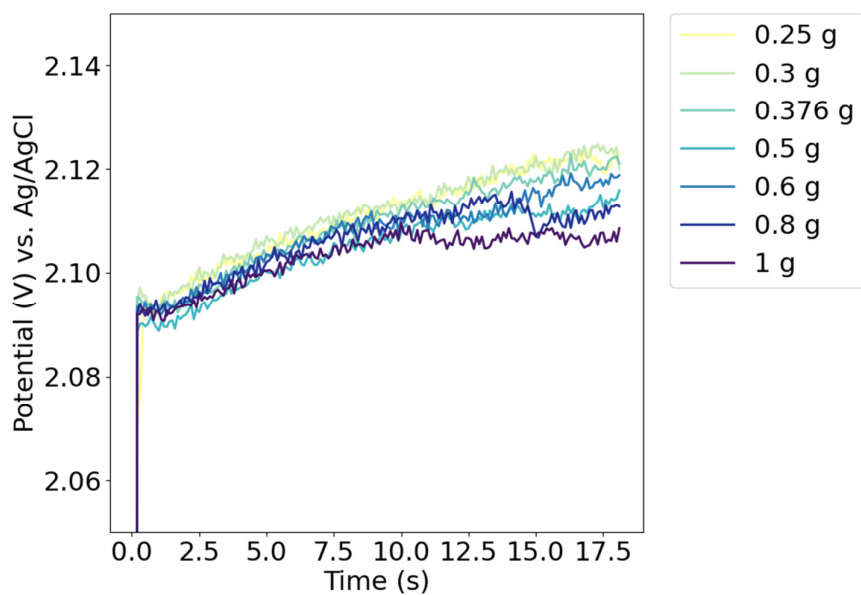
Supplementary Figure 14: Stills from video footage of the electrode at various times for 0-1 g. A comparison of the bubble formation during electrolysis ($t = 0-18$ seconds) at 50 mA cm^{-2} under reduced gravity conditions. Three examples of different experiments in microgravity (left) show that bubble retention on the electrode surface increases as buoyancy forces become less important.



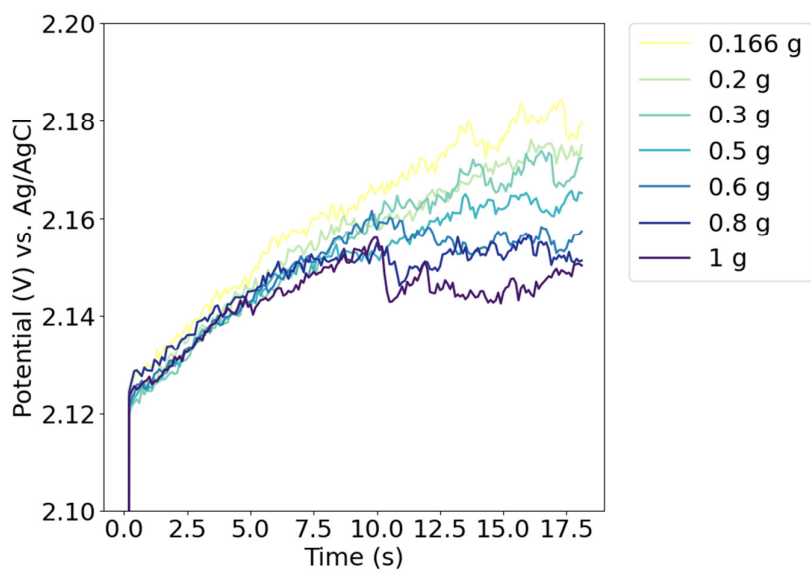
Supplementary Figure 15: Effect of g-jitter on small bubbles. Small bubbles impacted by g-jitter on an electrode at 8, 12, and 16 seconds during an electrolysis carried out at 100 mA cm^{-2} in microgravity during parabolic flight.



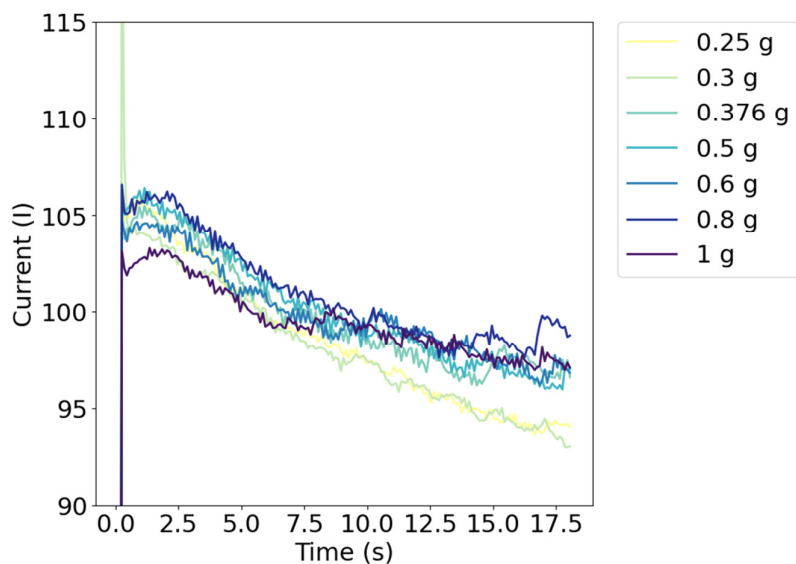
Supplementary Figure 16: Example raw V-t data at 50 mA cm⁻². An example reduced-gravity data set collected using chronopotentiometry at 50 mA cm⁻². Source data are provided as a Source Data file.



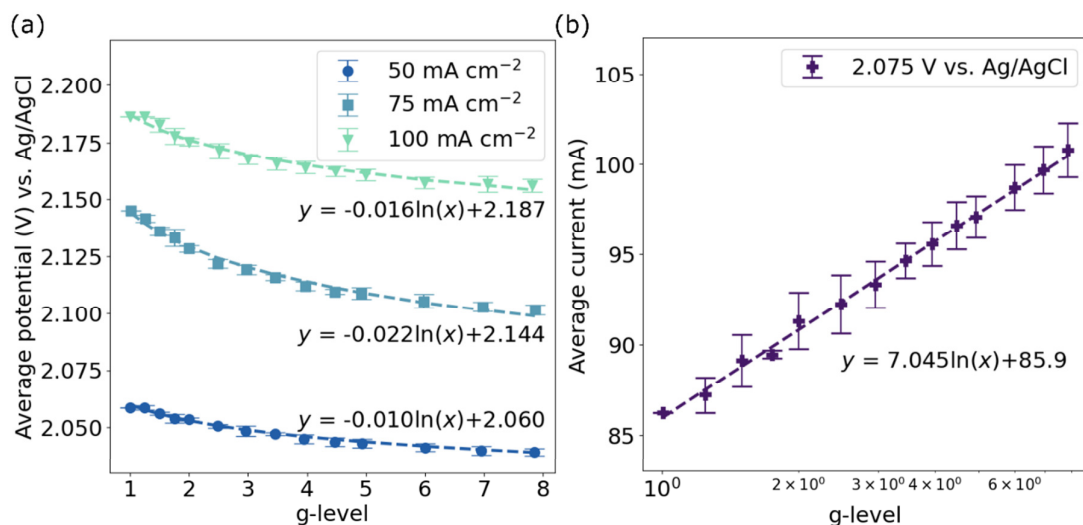
Supplementary Figure 17: Example raw V-t data at 75 mA cm⁻². An example reduced-gravity data set collected using chronopotentiometry at 75 mA cm⁻². Source data are provided as a Source Data file.



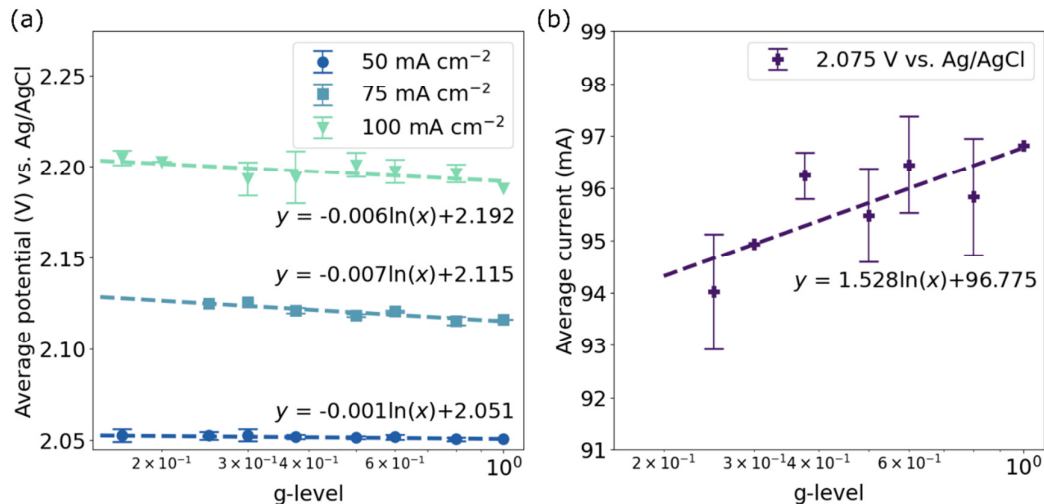
Supplementary Figure 18: Example raw V-t data at 100 mA cm^{-2} . An example reduced-gravity data set collected using chronopotentiometry at 100 mA cm^{-2} . Source data are provided as a Source Data file.



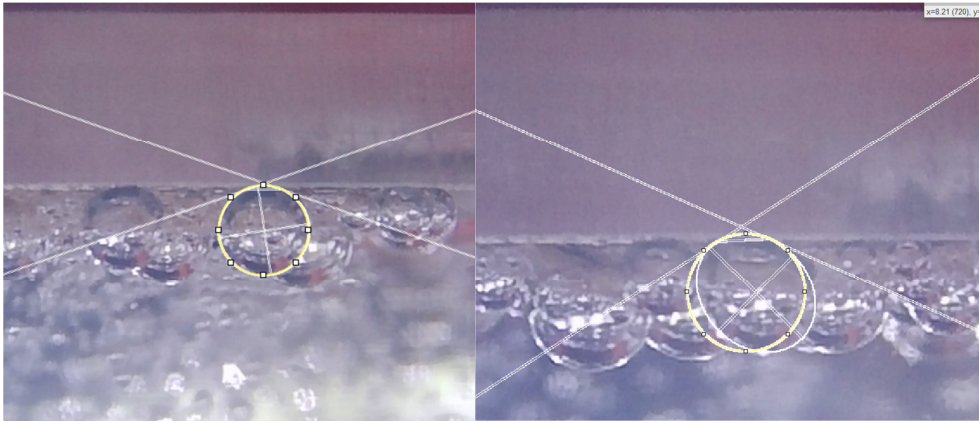
Supplementary Figure 19: Example raw i-t data at 2.075 V . An example reduced-gravity data set collected using chronoamperometry at 2.075 V vs. Ag/AgCl. Source data are provided as a Source Data file.



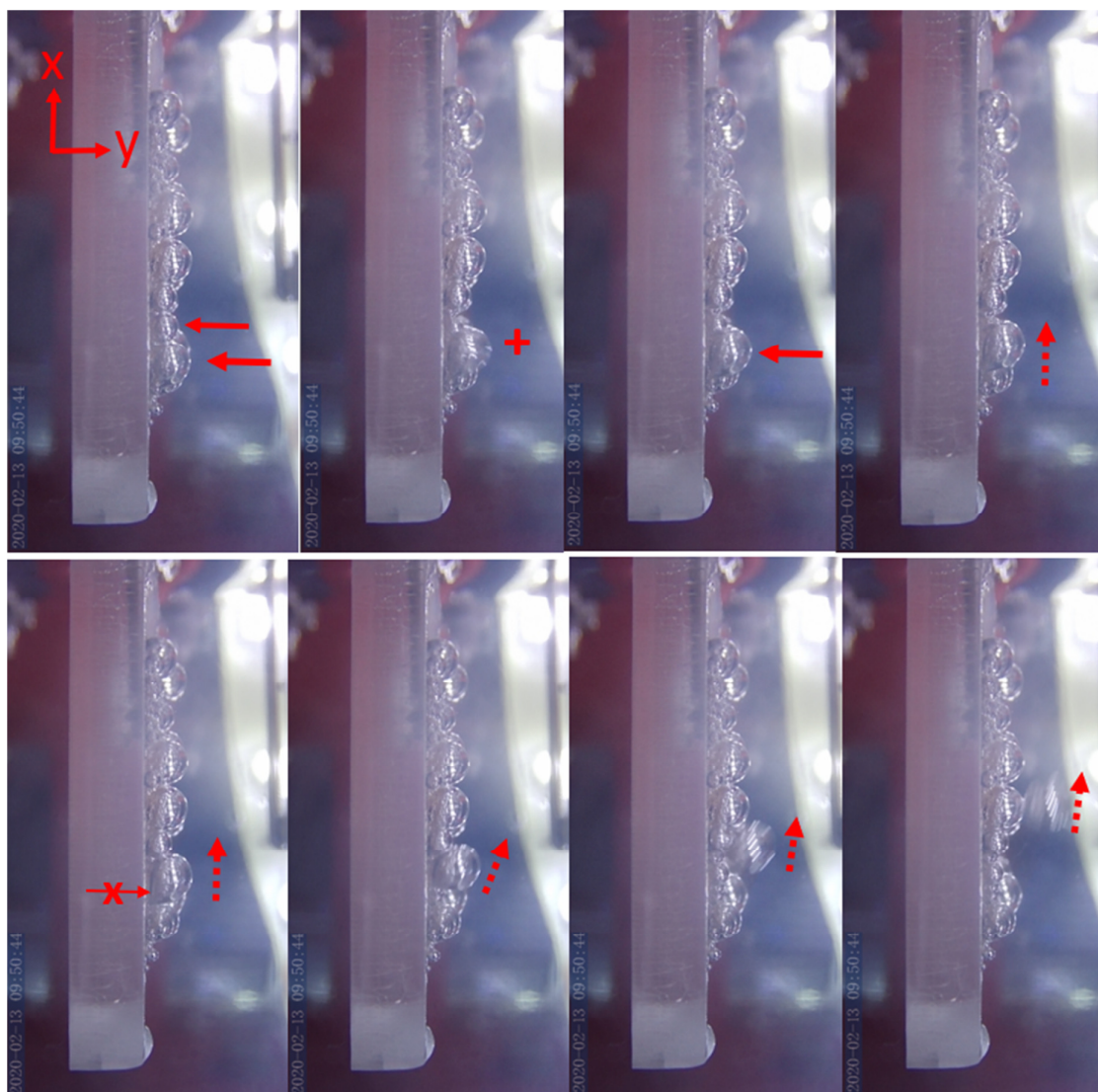
Supplementary Figure 20: Hypergravity gas-evolving electrolysis (1 – 8 g) data (Figure 2 in main text) displayed on a logarithmic scale. The average potential during galvanostatic experiments (a) and average current during potentiostatic experiments (b) with hypergravity conditions achieved using a centrifuge. Error bars represent the standard error of the mean. R^2 values are >0.98 for all the fitted trends shown. Source data are provided as a Source Data file.



Supplementary Figure 21: Reduced gravity gas-evolving electrolysis (0 - 1 g) data (Figure 3 in main text) displayed on a logarithmic scale. Figure 3 displayed on a logarithmic scale: The average potential or current of all reduced-gravity electrolysis experiments under galvanostatic (a) and potentiostatic (b) control, respectively, collected with the centrifuge. Error bars represent the standard error of the mean. Trends shown are calculated based on centrifuge data only and have an R^2 value of 0.848, 0.868, and 0.496 for 50, 75, and 100 mA cm⁻² respectively, and 0.651 for 2.075 V. Source data are provided as a Source Data file.



Supplementary Figure 22: Example contact angle data. An example of the ImageJ contact angle measurement for a bubble at microgravity (left) and 1 g (right)



Supplementary Figure 23: Bubble behavior on the electrode surface. One medium-large bubble and one smaller bubble coalesce, within <1 second the larger bubble that forms becomes unstable and slides along the face of the electrode. Here the force balance in the x direction is in the favour of buoyancy/departure. Then, once the advancing angle (the one at the back growing larger) is unsustainable, detachment occurs there initially, and the bubble then lifts off the surface in the y direction. Images are ordered sequentially left to right, where the second row follows directly from the end of the first row.

Supplementary Table

Supplementary Table 1: Average advancing and receding contact angles for oxygen bubbles on the gold electrode surface. Angles were measured in 1 g ($n = 8$) and micro-g ($n = 8$) conditions; angle labels correspond to those shown in Figure 6. The values shown in parentheses are the standard errors of the corresponding means.

	1 g			0 g		
	θ_a (°)	θ_r (°)	$\theta_a - \theta_r$ (°)	θ_a (°)	θ_r (°)	$\theta_a - \theta_r$ (°)
6 seconds	39.81 (2.21)	38.11 (1.60)	1.70	28.02 (1.67)	28.04 (1.50)	-0.02
16 seconds	48.53 (6.07)	40.65 (5.31)	7.88	19.85 (0.92)	19.94 (0.98)	-0.09
Average	41.78			23.96		

Supplementary Notes

Supplementary Note 1

The first thing to consider when assessing the quality of data obtained on the short-arm centrifuge is the accuracy of the artificial g-levels created. On a short-arm centrifuge system, variation in radius can have a significant impact on the g-level; the calculated gravity gradient across the electrode is shown for all reduced- and hyper- gravity levels targeted on the centrifuge in Supplementary Figures 6 and 7, respectively. Assessment of the gravity gradient shows that no two-target g-levels overlap; a maximum Δg of 0.4 g when 8 g is created can be anticipated during the hypergravity experiments, and a maximum Δg of 0.049 g can be anticipated when 1 g is generated by the centrifuge during reduced-gravity experiments. The measured g-level is the maximum value across the electrode face. The measured acceleration experienced by the cell in the z-axis (parallel to the face of the electrode) is shown in Supplementary Figures 4 and 5 for hypergravity and reduced-gravity data respectively. Overall, the mean g-level achieved with the short-arm centrifuge was very close to the targeted values due to the successful control of the motor rotation rate via a closed PID feedback loop with the cell accelerometer. Error bars representing two standard deviations show that the spread of data around the mean generally increases with increasing g-level due to increasing vibration. While the error bars are partially overlapping between adjacent g-levels, they are never entirely concurrent, indicating that the experimental g-levels were distinct.

Supplementary Note 2

The vibrational intensity in all three axes for each g-level studied is quantified and compared in Supplementary Figure 9. The electrochemical cell on the short-arm centrifuge experienced a maximum vibrational intensity when rotating to create 4 g, with the faster rotational speeds appearing to stabilize the centrifuge arms slightly. Vibration levels in reduced-gravity experiments were significantly lower and more consistent than hypergravity experiments. The shaking motion of the cells may improve mass transport in the electrolyte and could influence the bubble detachment behavior. It has been shown that, while application of ultrasonic vibration can enhance hydrogen evolution, it in fact hinders oxygen evolution by limiting the coalescence and detachment of bubbles [1]. The frequency of the vibrations in the present study was approximately 5 - 8 Hz. This is evidently several orders of magnitude different to the ultrasonic vibration used in the aforementioned study, however, that work highlights that the relationship between the hydrodynamic behavior of bubbles and vibrations is complex and is highly dependent on the specifics of an electrochemical system such

as electrode surface properties, the gas and electrolyte composition, and their interaction at the three-phase boundaries.

To assess whether the low frequency vibration experienced by the electrochemical cells may have influenced the trends in electrochemical efficiency seen in the present study, data was collected at 75 mA cm^{-2} on an orbital shaking plate rotating between 0 and 150 RPM. The vibrational intensity was comparable to the centrifuge data and is shown for all three axes in Supplementary Figure 10. The calculated average peaks per second varied between 8 and 14 Hz across the data set, which is on the same order of magnitude as that seen on the short-arm centrifuge. Supplementary Figure 10 shows that the average potential of data collected with a fixed current density of 75 mA cm^{-2} varies by less than 10 mV and does not follow a clear trend with the increasing vibration. The total variation between 1 – 8 g in Figure 2 in the main text is between 20 and 45 mV. While any level of varying vibration may influence electrochemical data, the comparison with data on the orbital shaking plate confirms that it cannot entirely account for the electrolysis trends that were identified.

Supplementary Note 3

Additionally, it was important to exclude a change in electrolyte composition as the primary cause for the gravity-dependent trend. While variation is unavoidable as Cu is removed from the electrolyte at the cathode and H^+ is generated at the anode, the electrolyte concentrations were chosen such that the excess of these species would mean that the change across a set of 15 experiments would be as small as possible. The upper limitations were solubility and flight safety regulations for the concentrations of copper sulfate and sulfuric acid, respectively. Supplementary Figure 11 shows hypergravity data collected at 100 mA cm^{-2} where the g-level was varied in both ascending and descending order. The same trend is seen in all data sets, with two ascending and one descending set following an almost identical logarithmic fit. One descending data set has a slightly shallower trend, indicating that the potential may slightly decrease over time in the system, but not enough to account for the trends seen in the hypergravity data, which validates the use of the chosen electrolyte composition to limit concentration variation. This data was collected with the highest current density used in this work; therefore, the effect would theoretically be lesser at all other current densities. As discussed in the main text, the shifted baselines seen in Supplementary Figure 11 are most likely due to small differences between the electrodes in each individual cell; this shift can be accounted for when considering the percentage change relative to 1 g in an individual dataset.

Supplementary Note 4

Other forces specific to centrifuge systems should be considered when using a short-arm centrifuge, such as the contribution of shear forces as gravity changes laterally across flat surfaces [2]. As the gas-evolving electrode face of interest was not horizontal relative to the axis of rotation but rather perpendicular to the plane of rotation and parallel to the radius, the impact of lateral shear forces can be considered negligible. Additionally, as the centrifuge is a spinning system, the Coriolis force could potentially influence the bubble behavior following detachment from the electrode surface. As such, all experiments were conducted with the gas-evolving electrode facing away from the direction of rotation so detached bubbles were less likely to disturb the electrode surface if influenced by the Coriolis force.

Flight data may also be affected by the bubble attachment behavior observed in reduced-gravity. The contact angle of a bubble on a vertical surface under low-gravity conditions is smaller than at higher g due to lower hydrostatic pressure; additionally, less vertical buoyancy force results in less difference between the advancing and receding contact angles [3], [4], [5]. The interfacial tension force that contributes to keeping a bubble attached to a surface is a function of the contact angles and contact diameter [6]. It is feasible that the lower interfacial tension force in reduced-gravity conditions means that the bubbles are more susceptible to influence from external factors, such as vibration from the centrifuge or g -jitter from the aircraft, which could preferentially expedite detachment of smaller bubbles. Additionally, as the cells were fixed in a horizontal orientation, the transition from 2 g to microgravity at the start of each parabola resulted in the complete reorientation of the electrolyte just prior to electrolysis. This sloshing motion may have impacted the results by introducing flow in the electrolyte and improving mass transport in the cell. If the impact of external factors on detachment was greater at lower g -levels, that would serve to oppose the influence of reduced buoyancy force and could dampen the apparent loss of efficiency at lower g -levels. Further work in more stable reduced-gravity conditions, such as those offered by a drop-tower, could potentially reduce this source of error.

Supplementary Note 5

Video footage suggests that g -jitter during the microgravity parabolas helped to dislodge smaller bubbles from the surface prematurely. Supplementary Figure 15 shows sequential images of bubbles during an experiment in microgravity, where the small bubbles are dislodged from the surface while the larger bubbles are less impacted. As some of the bubbles, particularly the smaller ones, are not attached to the surface but rather floating in the vicinity of the electrode, they will generate less

ohmic resistance. Previous microgravity studies in a drop tower have found the ohmic resistance at a gas-evolving electrode to increase steadily over time as more bubbles accumulate at the surface and block the electrode [7], [8]. In the present work, no significant increase in resistance over the course of an experiment was seen in microgravity. While microgravity electrolysis was not the primary focus of the present study, this effect may also be present in the reduced-gravity data. Further, these results highlight why the majority of microgravity electrolysis work is carried out in drop towers rather than parabolic flights, as a much higher quality of microgravity is possible with drop towers [7], [8], [9], [10].

Supplementary Note 6

ImageJ Contact Angle plug-in (<https://imagej.nih.gov/ij/plugins/contact-angle.html>) was used to investigate the contact angle of bubbles in different gravity levels. First, ImageJ was calibrated with the known thickness of 3 mm for the electrode holder. Then, the two contact points of the bubble with the surface were selected, before 5 further points were selected along the bubble perimeter. The plug-in then calculates both advancing (left) as well as receding (right) contact angles by using the sphere approximation ($\vartheta = 2\text{atan}(2h/l)$). The plug-in provides the internal angles, which would be relevant to a liquid drop, therefore, the supplementary angle was calculated to be relevant for the submerged bubble. Each bubble was measured three times and an average of these measurements was used. Then the mean and standard errors of the advancing and receding contact angles were calculated for 0 g and 1 g at 6 and 16 seconds, which is the data displayed in Table 1. An example of such analysis can be seen in Supplementary Figure 22.

Supplementary Note 7

Bubbles can be removed from the electrode in two ways. Bubble sliding, in which the bubble remains attached to the electrode, is the process by which a bubble slides vertically along the electrode until it meets the free surface. Secondly, bubbles can be removed from the electrode via the process of bubble detachment. During bubble detachment, bubbles, under the influence of buoyancy, neck and subsequently detach from the electrode and rise through the free liquid. These two processes can also both occur in succession, where a bubble first slides and subsequently lifts off the surface, as can be observed in Supplementary Figure 23. In microgravity, bubbles of roughly the same diameter following coalescence were stable on the surface and did not slide or lift off. When a bubble forms and grows on a surface which is not horizontal, it will grow asymmetrically and possibly slide along the inclined surface, while remaining attached [11]. The moment and bubble size

at which bubble sliding starts are dependent upon fluid properties (such as surface tension) and solid properties (such a surface energy and surface roughness). When bubbles slide vertically along the electrode's surface up to the free surface, they will coalesce with other bubbles, thus increasing bubble removal rate. Das et al. have shown that bubble sliding velocity and frequency of bubble sliding increases as the gravity vector increases [12]. This is caused by the increased buoyance force with increased gravitational acceleration. So, as gravity is decreased, bubble sliding frequency and velocity both decrease. Therefore, the bubble removal rate and electrolysis efficiency both decrease.

Supplementary Note 8

Past work has attempted to use various dimensionless quantities to scale bubble behavior across gravitational acceleration levels. However, the bubble behavior observed in the reduced gravity experiments cannot be fully accounted for with traditional scaling techniques. Pamperin, for example, used the Weber number to study bubble detachment from a submerged orifice in reduced gravity [13]. The Weber number is the ratio of inertial forces to cohesion forces (surface tension) acting on a multiphase flow (Eqn. 1) [13]. Although surface tension forces are expected to be significant in the reduced-gravity experiments described within this paper, the Weber number is not germane to the work described herein. The Weber number does not account for the change in gravitational acceleration. Secondly, bubbles nucleating, growing, and detaching through the process of electrolysis have minimal inertial forces acting upon them. Pamperin's experiments, by contrast, studied bubble detachment via gas jetting through an orifice [13].

$$We = \frac{\rho v^2 l}{\sigma} \quad (1)$$

The Grashof number might also be a candidate dimensionless quantity to scale fluid flows across gravity levels. The Grashof number is a ratio of buoyant to viscous forces acting on a fluid flow (Eqn. 2) [14]. While it is relevant to buoyant flows, the Grashof number is typically used to study single-phase flows experiencing natural convection, caused by temperature gradients. In contrast, the experiment conducted for this research aimed to maintain constant temperatures. The buoyant flows, instead, were caused by the electrolytic nucleation of gas bubbles. Lastly, the research conducted herein did not study the influence of viscosity (the second main term in the Grashof number) on bubble nucleation and growth.

$$Gr = \frac{g \beta \Delta T l^3}{\nu^2} \quad (2)$$

The Froude Number is another dimensionless quantity frequently used to characterize the influence of gravity on a fluid flow. The Froude number is the ratio of inertial forces to external body forces, often simply defined as the body force due to gravity (Eqn. 3) [15]. It is interesting to note that the Froude number scales nonlinearly with gravity, similar to the nonlinear relationship found in the research discussed in this paper. However, similarly to the Weber number, the Froude number's main parameter focuses on a flow's inertial forces. Since electrolytic bubble nucleation and growth occur in a non-flowing liquid, the Froude number does not completely apply to our work.

$$Fr = \frac{u}{\sqrt{g l}} \quad (3)$$

Finally, the Bond Number is perhaps the most frequently used dimensionless quantity when attempting to characterize bubble and droplet behavior, especially bubble shape. The Bond Number is the ratio of gravitational to surface tension forces (Eqn. 4) [16]. The Bond Number appears very applicable to the problem being studied: accounting for both the buoyant and surface-tension forces acting on the bubbles. However, there remain some important limitations to the use of the Bond Number. First, the Bond Number makes the assumption that the bubble is completely surrounded by liquid. That is, the Bond Number fails to account for any solid-fluid interactions. It has been shown that the properties of the solid, on which the bubble is adhered, can greatly influence the detachment time and volume of the bubble [10,17-20]. Since electrolysis efficiency is directly related to the release of bubbles from the electrode, the properties of the solid electrode, such as surface roughness or surface energy, must be accounted for in any dimensionless quantity used to scale across gravity levels. Finally, the Bond Number suggests a linear relationship as bubble behavior is scaled across gravity levels. The experimental trends presented in this research run counter to this, by displaying a nonlinear, logarithmic relationship between electrolysis efficiency and gravity level. Hence a dimensionless number that can accurately capture all the features required for modeling the behavior observed in this work, including the properties of the solid phase, has yet to be developed.

$$Bo = \frac{\Delta\rho g l^2}{\gamma} \quad (4)$$

Supplementary References

- [1] S. De Li, C. C. Wang, and C. Y. Chen, "Water electrolysis in the presence of an ultrasonic field," *Electrochim. Acta*, vol. 54, no. 15, pp. 3877–3883, Jun. 2009, doi: 10.1016/j.electacta.2009.01.087.
- [2] J. J. W. A. Van Loon, E. H. T. E. Folgering, C. V. C. Bouten, J. P. Veldhuijzen, and T. H. Smit, "Inertial shear forces and the use of centrifuges in gravity research. What is the proper control?," *J. Biomech. Eng.*, vol. 125, no. 3, pp. 342–346, Jun. 2003, doi: 10.1115/1.1574521.
- [3] A. Taqieddin, R. Nazari, L. Rajic, and A. Alshawabkeh, "Review—Physicochemical Hydrodynamics of Gas Bubbles in Two Phase Electrochemical Systems," *J. Electrochem. Soc.*, vol. 164, no. 13, pp. E448–E459, 2017, doi: 10.1149/2.1161713jes.
- [4] A. I. Rusanov, N. E. Esipova, and V. D. Sobolev, "Strong Dependence of Contact Angle on Pressure," *Dokl. Phys. Chem.*, vol. 487, no. 1, pp. 87–90, Jul. 2019, doi: 10.1134/S0012501619070017.
- [5] N. E. Esipova, A. I. Rusanov, V. D. Sobolev, and S. V. Itskov, "The Influence of Hydrostatic Pressure on the Contact Angle of a Sessile Bubble," *Colloid J.*, vol. 81, no. 5, pp. 507–514, Sep. 2019, doi: 10.1134/S1061933X1905003X.
- [6] D. Zhang and K. Zeng, "Evaluating the behavior of electrolytic gas bubbles and their effect on the cell voltage in alkaline water electrolysis," *Ind. Eng. Chem. Res.*, vol. 51, no. 42, pp. 13825–13832, Oct. 2012, doi: 10.1021/ie301029e.
- [7] D. Kiuchi, H. Matsushima, Y. Fukunaka, and K. Kuribayashi, "Ohmic Resistance Measurement of Bubble Froth Layer in Water Electrolysis under Microgravity," *J. Electrochem. Soc.*, vol. 153, no. 8, p. E138, 2006, doi: 10.1149/1.2207008.
- [8] G. Sakuma, Y. Fukunaka, and H. Matsushima, "Nucleation and growth of electrolytic gas bubbles under microgravity," *Int. J. Hydrogen Energy*, vol. 39, no. 15, pp. 7638–7645, 2014, doi: 10.1016/j.ijhydene.2014.03.059.
- [9] H. Matsushima, T. Nishida, Y. Konishi, Y. Fukunaka, Y. Ito, and K. Kuribayashi, "Water electrolysis under microgravity: Part 1. Experimental technique," *Electrochim. Acta*, vol. 48, no. 28, pp. 4119–4125, 2003, doi: 10.1016/S0013-4686(03)00579-6.
- [10] K. Brinkert *et al.*, "Efficient solar hydrogen generation in microgravity environment," *Nat. Commun.*, vol. 9, no. 1, 2018, doi: 10.1038/s41467-018-04844-y.
- [11] Das, A.K., and Das, P.K., "Bubble evolution and necking at a submerged orifice for the complete range of orifice tilt," *AIChE Journal*, Vol. 59, No. 2, 2013, pp. 630-642.
- [12] Das, S., Weerasiri, L.D., and Yang, W., "Influence of surface tension on bubble nucleation, formation and onset of sliding," *Colloids and Surfaces A: Physicochemical and Engineering Aspects*, Vol. 516, 2017, pp. 23-31.
- [13] Pamperin, O., and Rath, H., "Influence of buoyancy on bubble formation at submerged orifices," *Chemical Engineering Science*, Vol. 50, No. 19, 1995, pp. 3009-3024.
- [14] Bergman, T.L., Lavine, A.S., Incropera, F.P., "Fundamentals of Heat and Mass Transfer," Wiley, Somerset, 2011, pp. 408.
- [15] White, F.M., and Xue, H., "Fluid mechanics," McGraw-Hill, New York, NY, 2021, pp. 294.

- [16] Clift, R., Grace, J.R., and Weber, M.E., "Bubbles, drops, and particles," Acad. Pr, New York, NY [u.a.], 1978, pp. 26.
- [17] Burke, P.A., and Dunbar, B.J., "Development of Computational Fluid Dynamic (CFD) Models of the Formation and Buoyancy-Driven Detachment of Bubbles in Variable Gravity Environments," *AIAA Scitech 2021 Forum* (2021). DOI: 10.2514/6.2021-1838.
- [18] Sakuma, G., Fukunaka, Y. & Matsushima, H. "Nucleation and growth of electrolytic gas bubbles under microgravity". *Int. J. Hydrogen Energy* 39, 7638–7645 (2014).
- [19] Xu, W., Lu, Z., Sun, X., Jiang, L. & Duan, X. "Superwetting Electrodes for Gas-Involving Electrocatalysis". *Acc. Chem. Res.* 51, 1590–1598 (2018).
- [20] Zhao, X., Ren, H. & Luo, L. "Gas Bubbles in Electrochemical Gas Evolution Reactions." *Langmuir* 35, 5392–5408 (2019).